

Large language models reorganize representational geometry during in-context learning

Hua-Dong Xiong¹, Li Ji-An², Robert C. Wilson^{1,3}, Kwonjoon Lee^{4*}, Xue-Xin Wei^{5*}

¹ School of Psychological and Brain Sciences, Georgia Tech

² Department of Psychology, New York University

³ Center of Excellence for Computational Cognition, Georgia Tech

⁴ Honda Research Institute

⁵ Departments of Neuroscience and Psychology, The University of Texas at Austin

Abstract

Large language models (LLMs) exhibit remarkable flexibility: they can adapt to novel tasks from in-context examples without any parameter updates, a capability known as in-context learning (ICL). Prior work on synthetic tasks has shown that ICL can implement specific algorithms, demonstrating architectural competence, and mechanistic analyses have identified key circuits that support this behavior. However, because in-context computation — regardless of its algorithmic form — relies on transformations in high-dimensional representation space, it remains unclear how the geometry of that space shapes ICL effectiveness. Motivated by the neuroscience view of classification as the untangling of neural representations, we hypothesize that ICL depends on the successful online untangling of task-relevant representations. To test this idea, we study how LLMs classify in-context examples whose labels are defined by the model’s own internal representations with known structure. We show that ICL performance correlates systematically with the representational structure of the underlying classification task and that successful ICL is accompanied by geometric reorganization that increases online separability. We further find that LLM behavior is well described by a prototype-like algorithm that integrates evidence while reshaping representations to support classification. These findings offer a geometric account of ICL in pretrained LLMs, establish representational geometry as a mechanistic constraint on ICL, and quantify the gap between what pretrained representations afford and what in-context learning can exploit.

1 Introduction

Large language models (LLMs) can rapidly adapt to new tasks from demonstrations without parameter updates—a capability known as in-context learning (ICL) (Brown et al., 2020). Despite its practical success, it remains unclear what computations underlie ICL in pretrained models and what determines whether ICL succeeds or fails. Prior work has linked ICL to online gradient-based optimization (Ahn et al., 2023; Cheng et al., 2024; von Oswald et al., 2023a;b), Bayesian inference (Müller et al., 2021; Reuter et al., 2025; Xie et al., 2022), and related statistical procedures (Bai et al., 2023; Chen & Wang, 2022; Dherin et al., 2025; Garg et al., 2022). However, most of this evidence comes from training small transformers on synthetic tasks, showing what the architecture can implement under tailored training rather than what pretrained LLMs actually do in naturalistic settings. Other studies identify circuit motifs essential to ICL—such as induction heads (Olsson et al., 2022; Wang et al., 2022) and function vectors (Hendel et al., 2023; Todd et al., 2024)—yet these do not explain what makes an in-context task easy or hard (Wei et al., 2023).

*Co-senior author

A central challenge in studying ICL in pretrained LLMs is distinguishing genuine online inference of the task rule from reliance on spurious semantic or statistical correlations. When labels align with familiar categories, models may appear to learn from demonstrations while actually exploiting superficial label–feature associations acquired during pretraining, rather than inferring the task rule from the provided examples. This concern is compounded by ICL’s sensitivity to the choice, ordering, and formatting of demonstrations (Liu et al., 2024; Wang et al., 2024; Wei et al., 2023; Zhao et al., 2021), which further obscures what drives performance.

Here we propose a representational-geometry account of ICL. Building on the neuroscience view of classification as the untangling of neural representations (DiCarlo & Cox, 2007; DiCarlo et al., 2012; Yamins & DiCarlo, 2016) (Fig. 1), we ask whether successful ICL in pretrained LLMs can be understood as the online untangling of task-relevant internal representations. To test this idea, we define a controlled family of in-context classification tasks in which labels are given by binary linear partitions of the model’s internal representations. By varying these partitions along principal component directions from high to low variance, we induce a smooth difficulty gradient grounded in the model’s own representational structure rather than human-curated labels. Because the labels are derived from the model’s own representation space rather than from familiar semantic categories, this design reduces semantic confounds and provides a cleaner setting for studying how pretrained LLMs exploit their internal representational geometry during ICL.

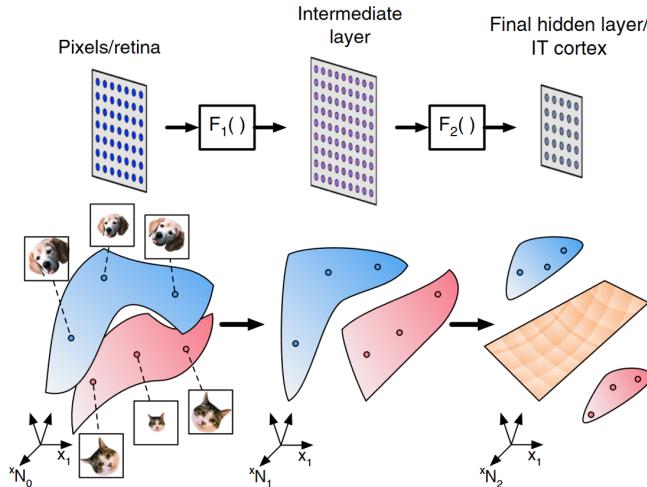


Figure 1: **Classification as untangling neural representations.** Raw sensory inputs (e.g., at the retina) initially give rise to highly entangled representations, in which category manifolds are not yet linearly separable. Through successive stages of processing, both visual cortex and deep networks progressively untangle these representations so that category manifolds become increasingly linearly separable in later layers (adapted from Cohen et al. (2020)) and easier to read out.

To characterize the dynamics of ICL under this framework, we analyze how the geometry of the induced class manifolds evolves as in-context examples accumulate. We quantify changes in separability, radius, dimensionality, and signal-to-noise ratio, and we compare the model’s behavior with a suite of online learning algorithms operating over the same internal representations.

Our main findings are threefold. First, ICL performance depends strongly on the geometry of the task-defining partition: labels aligned with high-variance representational directions are learned more successfully than those defined along low-variance directions. Second, successful ICL is accompanied by online geometric reorganization of final-layer representations, including increased separability and signal-to-noise ratio. Third, the model’s behavior is best captured by a prototype-based learner, suggesting that in this setting LLMs compress contextual evidence into class-level summaries rather than implementing a near optimal online inference algorithm.

Together, these findings suggest that ICL success is both constrained by and reflected in the geometry of a model’s internal representations. The representation-defined ICL paradigm and accompanying geometric analysis framework provide new tools for probing the mechanisms of ICL in pretrained LLMs.

2 Methods

2.1 Representation-defined in-context classification task

We construct a family of in-context classification tasks whose labels are defined directly from the model’s hidden states (Ji-An et al., 2025) (Fig. 2). Let $D = \{x_i\}_{i=1}^N$ denote a dataset of sentences and let M denote the evaluated LLM. For each target layer ℓ , the model maps each sentence x_i to a sentence-level representation $h_i^{(\ell)} \in \mathbb{R}^d$. We then construct a set of candidate axes $\mathcal{W}(D, M, \ell) \subset \mathbb{R}^d$ from these representations. Each pair (ℓ, w) , where $w \in \mathcal{W}(D, M, \ell)$, defines a task instance $T_{\ell, w}$ through the binary label

$$y_i^{(\ell, w)} = \mathbf{1}[\langle w, h_i^{(\ell)} \rangle > 0].$$

Thus, each task is specified by a target layer ℓ and a task-defining axis w . The target layer determines the representation space from which labels are derived, and the task-defining axis determines the binary partition within that space. At evaluation time, the model is given n in-context examples $(x_1, y_1^{(\ell, w)}), \dots, (x_n, y_n^{(\ell, w)})$ and is asked to predict the label $y_{n+1}^{(\ell, w)}$ for a new sentence x_{n+1} (Fig. 2c; details in Appendix A.4).

We consider two axis families for the task-defining axis: LR and PCs. The LR family contains a single logistic-regression (LR) axis obtained by fitting a linear classifier from $h_i^{(\ell)}$ to the dataset labels, yielding a direction aligned with the dominant task-relevant structure already encoded in the model’s sentence representations. The PC family contains principal component (PC) directions from the same target-layer representation space. For a selected PC direction $w = \text{PC}_k$, labels are defined by the sign of the projection $\langle w, h_i^{(\ell)} \rangle$. Because the PC basis is computed from centered sentence representations, thresholding the projection at zero yields an approximately balanced binary partition. We consider $k \in \{1, 2, 4, 8, 32, 128, 512\}$. Because PCs are ordered by explained variance, they provide a principled axis family ranging from dominant to weak directions of variation in the model’s initial sentence representations. In this sense, variance indexes how strongly a direction participates in organizing the representation of the dataset according to the model’s pretrained features, allowing us to test which representational structure ICL can exploit online. We instantiate these tasks at five target layers spanning model depth, selected by evenly spaced layer quantiles (details in Appendix A.3.2). We refer to each target-layer/axis pair as a condition and evaluate 200 prompt-level trials per condition (details in Appendix A.3.3). Unless otherwise noted, reported summaries average across layers; analyses at individual target layers yield qualitatively similar patterns.

2.2 Models and datasets

We consider two complementary evaluation settings. First, we assess model-level generalization by aggregating results across eight instruction-tuned models: Llama3 (Grattafiori et al., 2024) (3B, 8B), Gemma3 (Gemma et al., 2025) (1B, 4B, 12B, 27B), and Qwen3 4B (Yang et al., 2025) and Qwen3.5 27B (Qwen, 2026). All models are evaluated on ETHICS-commonsense (Hendrycks et al., 2020). Second, to evaluate task-level generalization, we fix a single model, Qwen3 4B, and evaluate it across five sentence classification datasets: ETHICS-commonsense and ETHICS-justice (Hendrycks et al., 2020), SST-2 and CoLA from GLUE (Wang et al., 2018), and LIAR (Wang, 2017) (details in Appendix A.2).

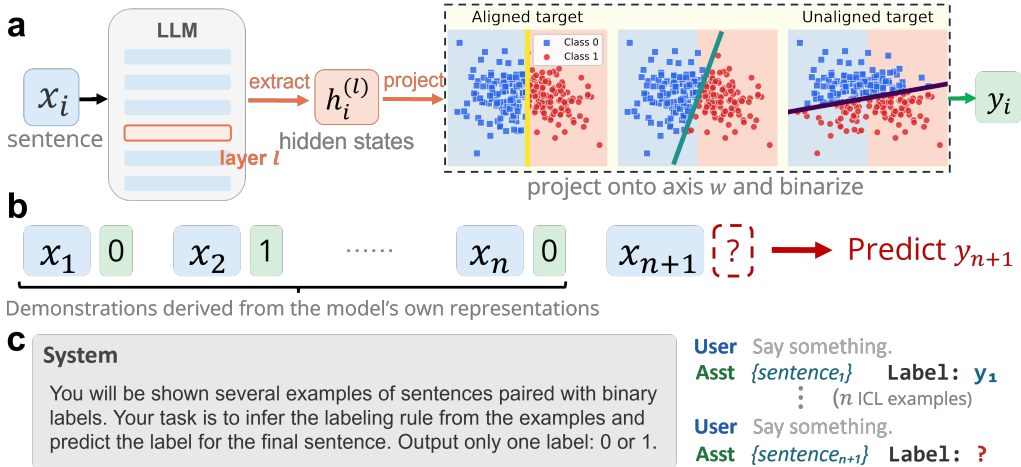


Figure 2: **Representation-defined in-context classification task.** (a) For each sentence x_i , we extract a sentence-level representation $h_i^{(\ell)}$ from a selected target layer ℓ , project it onto a task-defining axis w , and binarize it into a label y_i . Background shading shows the decision regions of the logistic-regression axis, aligned with the model’s pretrained semantics for the given dataset. Point colors indicate the labels assigned by the axis w ; as w becomes increasingly misaligned with the logistic axis, point labels diverge from the background partition. This procedure is instantiated at five target layers, uniformly sampled across model depth. (b) The model is then given a sequence of (sentence x_i , label y_i) pairs and asked to predict the label for a new sentence. (c) Example prompt.

3 Results

3.1 ICL performance varies across task-defining axes

We hypothesized that task-defining partitions aligned with stronger representational directions would be easier to infer from demonstrations. Under a representational-untangling account, this behavioral advantage should be accompanied by stronger online geometric reorganization of final-layer representations.

We find that ICL accuracy improves with the number of in-context examples, indicating that models use demonstrations to infer the task-defining partition rather than relying solely on structure already encoded in their pretrained weights (Fig. 3). This effect appears both on ETHICS-commonsense, averaged across eight pretrained LLMs (Fig. 3a), and for Qwen3 4B across five datasets (Fig. 3b). Consistent with our hypothesis, ICL performance depends strongly on the task-defining axis, and this pattern holds consistently across the five target layers. Axes aligned with high-variance representational directions—including leading principal components (PC1, PC2, PC4, and PC8) and the LR axis—yield substantially higher accuracy and faster improvements than those aligned with low-variance directions, such as trailing PCs (PC32, PC128, and PC512). These results reveal a controlled success-failure regime for ICL: partitions aligned with high-variance representational directions are substantially easier for LLMs to infer and reorganize in context than partitions defined along low-variance directions.

3.2 Geometric measures of representations

To directly test the untangling hypothesis, we quantify how final-layer representations reorganize during ICL using geometric measures of class manifolds. Specifically, we draw on manifold capacity theory (Chung et al., 2018; Cohen et al., 2020) and the signal-to-noise ratio (SNR) between manifolds (Sorscher et al., 2022). Capacity serves as a proxy for linear separability: higher capacity indicates that the two class manifolds can be more easily separated. In contrast, radius and intrinsic dimensionality capture aspects of within-class

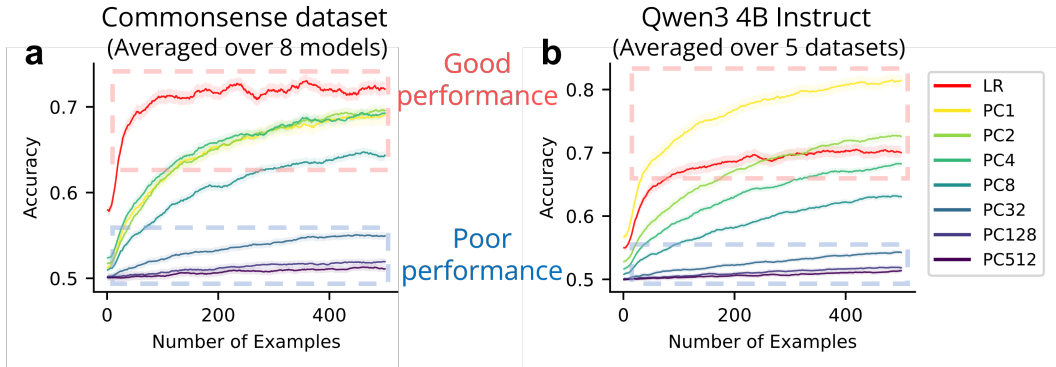


Figure 3: **In-context classification accuracy varies across task-defining axes.** In-context classification accuracy as a function of the number of in-context examples, showing graded separation between easy task-defining axes (the LR axis and leading PCs) and difficult task-defining axes (trailing PCs). **(a)** Accuracy averaged over five target layers sampled at evenly spaced depth quantiles and over eight models of varying sizes and families on ETHICS-commonsense. Shaded regions denote ± 1 standard error of the mean (SEM) across models. **(b)** Accuracy for Qwen3 4B averaged over the same five target layers and five datasets. Shaded regions denote ± 1 SEM across datasets.

spread—broader and higher-dimensional manifolds are more difficult to separate. SNR quantifies how clearly discriminative structure emerges from background variability (Fig. 4). For each of the five target layers ℓ and each task-defining axis (LR or PCk), we track these metrics over the induced class manifolds in the model’s final-layer representations across successive in-context learning steps (example index $t = 1, 2, \dots$), averaging each step over 200 runs. Because the qualitative patterns are consistent across layers, we report averages over the five target layers (formal definitions and implementation details are provided in Appendix A.7).

3.3 Online representational geometry reorganization during ICL

Why does ICL performance differ across task-defining axes? Under the untangling framework, one possibility is that improvement depends on whether the class partition defined can be reorganized into a more separable geometry in the model’s final-layer representations as in-context examples accumulate. If so, successful ICL should increase linear separability (higher capacity), reduce within-class complexity (lower radius and/or dimensionality), and thereby improve discriminability (higher SNR).

We test these predictions by systematically analyzing manifold capacity, radius, intrinsic dimensionality, and SNR as a function of the number of in-context examples (Fig. 5). These metrics are computed from final-layer representations and averaged over the five target layers and experimental runs for each task-defining axis.

For task-defining axes (the LR axis and leading PCs) with strong ICL performance, capacity increases while radius and intrinsic dimensionality decrease with the number of examples, so SNR rises sharply. This pattern indicates a progressive sharpening of the decision-relevant subspace in the final-layer readout. For more difficult task-defining axes (trailing PCs), these changes are substantially attenuated: capacity remains low, radius and dimensionality change little or even increase slightly, and SNR remains near zero, indicating limited movement toward a linearly separable configuration. These geometric outcomes closely mirror the success and failure regimes in Fig. 3. The same qualitative pattern holds across target layers and models, and also appears for Qwen3 4B across five datasets (Appendix Fig. 7).

Our analysis reveals that in-context learning is not a general-purpose algorithm that solves arbitrary tasks. Instead, it is constrained by representational geometry: the same in-context learning mechanism operates differently depending on the target layer and task-defining axis that define the task. Along trailing-PC task-defining axes, the model’s final-layer

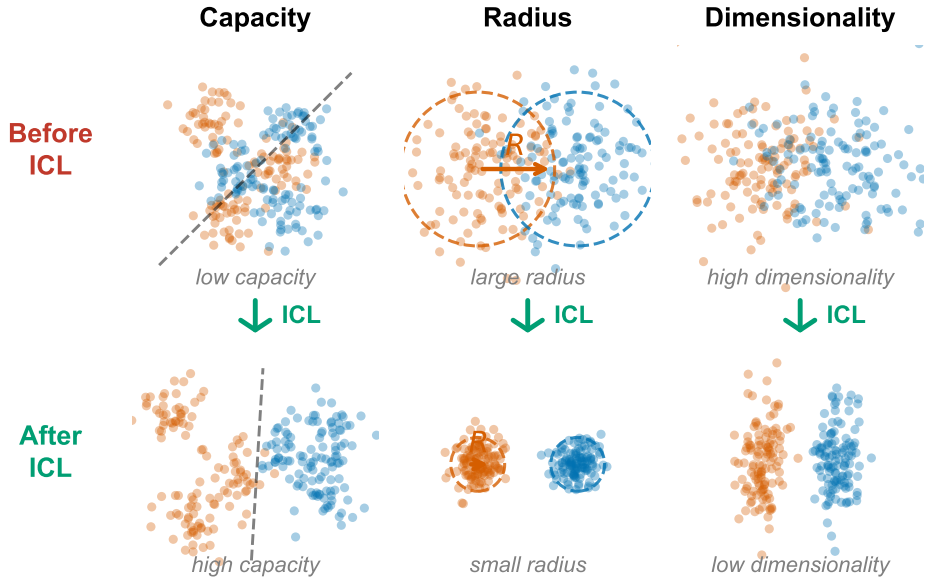


Figure 4: **Schematic of how neural manifold geometry shapes classification difficulty.** Each column illustrates one geometric property of class manifolds before (top) and after (bottom) successful in-context learning. *Capacity*: when class manifolds overlap (low capacity), linear classification is difficult; ICL separates the manifolds, yielding high capacity. *Radius*: large within-class spread hinders separation; ICL compresses each manifold, reducing radius. *Dimensionality*: high-dimensional within-class variability complicates separation; ICL contracts manifolds to fewer effective directions.

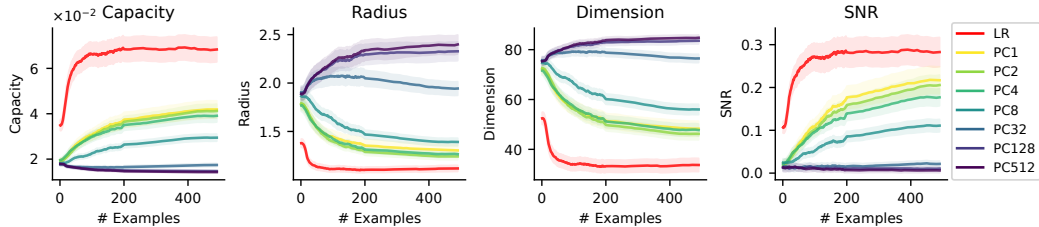


Figure 5: **Geometric reorganization of neural representations during ICL.** Capacity, radius, dimension, and SNR of the final-layer representations across in-context examples, averaged over five target layers and eight models. Each curve denotes a different task-defining axis. The LR axis and leading PCs (PC1/2/4/8) exhibit strong geometric reorganization with in-context examples, with increasing capacity and SNR and decreasing radius and dimension, whereas trailing PCs (PC32/128/512) remain in low-capacity, low-SNR regimes.

representations are comparatively resistant to the reorganization needed to support accurate in-context classification, even with many demonstrations. By contrast, the LR axis and leading PCs reliably induce the capacity increases, dimensionality reduction, and SNR gains expected from successful online untangling. ICL therefore appears to reflect a selective form of representational untangling that is more tractable along directions already salient in pretrained representational geometry.

3.4 Representational geometry predicts ICL performance

Finally, we quantify how well geometry predicts behavior by correlating ICL accuracy with final-layer geometry metrics across target layers, task-defining axes, in-context examples, and models on ETHICS-commonsense (Table 1). Here, each analysis unit is a specific combination of model, task-defining axis, target layer, and in-context example count; within each such

condition, accuracy and geometry metrics are computed across the set of repeated runs (details in Appendix A.7). Final-layer geometry strongly predicts performance: accuracy increases with manifold capacity ($r = 0.83$) and SNR ($r = 0.71$) and decreases with radius ($r = -0.78$) and especially dimension ($r = -0.87$). Thus, these metrics provide a compact geometric characterization of ICL success in this paradigm, directly linking behavioral accuracy to the structure of the final-layer representations.

Table 1: **Representational geometry explains ICL performance.** Pearson r between each geometric metric and ICL accuracy, aggregated across axes and in-context positions. *** $p < .001$.

| Capacity | Dimension | Radius | SNR |
|----------|-----------|----------|---------|
| 0.83*** | -0.87*** | -0.78*** | 0.71*** |

3.5 ICL behavior is best described by prototype learning on the representations

Having characterized ICL as representational reorganization, we next ask what online learning rule best describes the model’s behavior. We compare the LLM’s predictions to a set of simple online learning models that operate on the same final-layer representations (Fig. 6) to understand how past examples are represented and updated in the model.

These models differ mainly in what they store from the past and how they update it. Prototype learning summarizes each class by a single centroid, effectively treating multiple examples as a classwise abstraction rather than remembering them one by one. Exemplar learning instead retains all previous instances and compares a new example to the full memory. Our nearest-neighbor model is the simplest version of this idea: it predicts from the single closest stored instance (1-NN). Online gradient descent (OGD) instead maintains a linear decision rule and nudges its weights after each example in proportion to the current prediction error. The Bayesian class-mean model returns to class means, but treats them as uncertain latent variables and updates both the mean estimate and its uncertainty online. The Kalman filter shifts the latent state from class means to the weights of a linear decoder, updating both the decoder and its uncertainty with a gain that depends on how informative the current example is (details in Appendix A.8.3).

We evaluate how well each model predicts the LLM’s responses (descriptive fit; averaged across target layers, details in Appendix A.8.3). Prototype learning best matches the LLM’s output distribution (Fig. 6). This suggests that the LLM behaves like a centroid-based learner when the underlying final-layer representation supports reliable separation. By contrast, more flexible linear online learners can achieve higher task accuracy from the same representations, indicating that the LLM’s in-context update is prototype-like in behavior but not accuracy-optimal.

4 Discussion

In this work, we studied in-context learning (ICL) through the lens of representational geometry. Building on the neuroscience view of classification as the untangling of neural representations, we defined a family of in-context classification tasks directly in representation space, allowing us to test whether pretrained LLMs can untangle representations of experimenter-defined partitions derived from their own internal representations. We found that ICL success depends systematically on the geometry of the task-defining partition: tasks aligned with dominant representational directions are learned more successfully, and successful learning is accompanied by online geometric reorganization that makes final-layer representations progressively more separable. Together, these results suggest that ICL in pretrained LLMs can be understood as a selective online reorganization of representational geometry, constrained by structure inherited from pretraining.

Our findings complement prior work that interprets ICL in terms of online algorithms—mechanisms that transformers may implement during inference (Ahn et al., 2023; Cheng

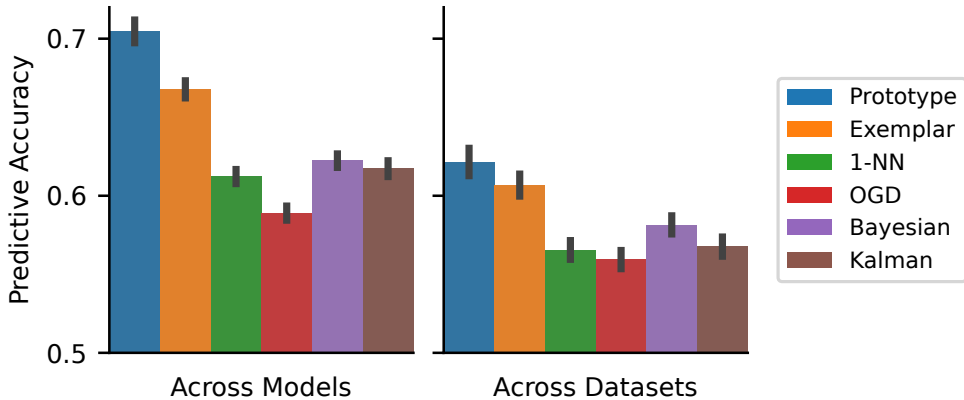


Figure 6: **Comparison of different online algorithms in predicting the response of LLMs.** Accuracy of six different online learners in predicting the LLM’s responses (descriptive fit), computed from final-layer representations and averaged over five target layers. The prototype model matches LLM behavior best. **(a)** Model fitting accuracy averaged over eight LLMs on ETHICS-commonsense. Shaded regions denote ± 1 SEM across models. **(b)** Model fitting accuracy for Qwen3 4B averaged over five datasets. Shaded regions denote ± 1 SEM across datasets.

et al., 2024; von Oswald et al., 2023a;b; Müller et al., 2021; Reuter et al., 2025; Bai et al., 2023; Xie et al., 2022). In contrast, our analysis focuses on ICL as it manifests in pretrained models, and our framework characterizes ICL behavior in terms of geometric properties of high-dimensional population responses. This perspective yields directly measurable geometric quantities that predict ICL performance and links ICL behavior to a simple prototype learning model that captures online geometric reorganization.

These results also sharpen a broader question: what are the limits of ICL, and to what extent can it support arbitrary input-output mappings? Some studies have identified architectural motifs—such as induction heads (Olsson et al., 2022; Wang et al., 2022) and function vectors (Hendel et al., 2023; Todd et al., 2024)—as critical to ICL. Yet these do not explain why some in-context tasks are easier or harder (Wei et al., 2023). Other work approaches the problem normatively, asking what training distributions make ICL feasible (Chan et al., 2022; Singh et al., 2024) and how in-context and in-weights learning interact (Anand et al., 2025; Russin et al., 2025). Our results provide a complementary mechanistic perspective: pretraining does not merely provide knowledge and task priors, but also establishes a representational substrate over which ICL operates. From this viewpoint, ICL is not a task-agnostic procedure whose success is independent of the representational substrate. Instead, its success depends on whether the task can be supported by the geometry of the pretrained representation space. In this sense, failure in ICL need not reflect insufficient supervision from context; it can also reflect a mismatch between the task and the representational structure inherited from pretraining.

Intuitively, for a given model M and dataset D , explained variance measures how strongly a direction participates in organizing the model’s pretrained representation space for that dataset. Leading PCs capture dominant axes of variation already present in the representation and therefore provide a more accessible substrate for online untangling during ICL: labels defined along these directions can be inferred more reliably from a small number of demonstrations and more readily reorganized into a linearly separable final-layer geometry. Trailing PCs, by contrast, contribute little to this representational backbone, yielding weaker and less stable evidence for the task-defining partition and making them correspondingly harder for the model to exploit in context. It would be interesting for future work to establish a formal theory based on these empirical observations.

Limitations. First, our tasks are deliberately constructed as representation-defined binary classification problems. This provides strong experimental control and makes it possible

to isolate representational constraints on ICL, but it remains unclear to what extent the same geometric principles generalize to richer task settings, including prediction, generation, or reasoning. Second, the task-defining partitions studied here are linear, whereas many real-world tasks may depend on more complex nonlinear structure. Third, although our choice of task-defining axis families is principled, it is not unique. We used logistic regression to identify salient label-related directions and principal components to define an ordered family of axes indexed by explained variance. These are useful probes of how ICL leverages pretrained structure, but they do not exhaust the possible notions of task-relevant geometry. Other choices—for example, random directions or nonlinear manifold coordinates—may reveal different constraints on ICL and offer finer experimental control.

Future directions. First, it remains unclear how far the prototype-like algorithmic signature we observe generalizes beyond the current task family. Although our cognitive-model comparison suggests that ICL in this setting is well described by a prototype-like learner—one that compresses contextual evidence into coarse class-level summaries that guide the reshaping of subsequent representations—this description may be incomplete or task-specific. More complex settings, including tasks with hierarchical feedback, structured latent variables, nonlinear category structure, or demands for maintaining a persistent belief state over long contexts, may require richer forms of in-context computation than prototype-like summarization. Second, our results suggest that the limits of ICL may arise not only from the representational substrate inherited from pretraining, but also from the form of the online update rule itself. This raises the possibility of treating improved in-context updating as a design target: whether pretrained LLMs can be trained or steered toward update rules that better exploit task-relevant representations, and whether doing so expands the regime in which geometric reorganization occurs. Third, an important open question is how the representational geometry that supports or limits ICL is shaped by training. If these constraints are inherited from pretraining, then a natural next step is to characterize how they emerge over the course of pretraining and how they are modified by instruction tuning or other forms of finetuning. This could help disentangle improvements in ICL that arise from better representations from those that arise from changes in the effective online update dynamics. Fourth, it remains important to understand how such update rules are mechanistically implemented in the network. Identifying which circuit motifs support prototype-like updating, and under what conditions they can support a more persistent latent belief state, would help connect representational geometry, algorithmic descriptions of ICL, and circuit-level mechanisms into a more unified account of how pretrained LLMs learn from context. Finally, it would be valuable to extend this framework to reasoning settings, especially those involving chain-of-thought prompting. One possibility is that additional generated tokens provide extra sequential computation that allows the model to further reorganize or untangle task-relevant representations before producing an answer.

Conclusion. We proposed a representational-geometry account of in-context learning in pretrained LLMs. Across a controlled family of representation-defined classification tasks, we showed that ICL success is systematically constrained by the geometry of the task-defining partition and that successful learning is accompanied by online reorganization of representations toward greater separability. These results suggest that pretraining does more than endow LLMs with knowledge that can be used in context: it also establishes the representational substrate that determines which task partitions can be effectively reorganized online. In this view, success and failure in ICL can be understood not only in terms of task statistics or algorithmic form, but also in terms of the evolving geometry of internal representations.

References

- Kwangjun Ahn, Xiang Cheng, Hadi Daneshmand, and Suvrit Sra. Transformers learn to implement preconditioned gradient descent for in-context learning. In *Advances in Neural Information Processing Systems*, volume 36, pp. 45614–45650, December 2023. URL https://proceedings.neurips.cc/paper_files/paper/2023/hash/8ed3d610ea4b68e7afb30ea7d01422c6-Abstract-Conference.html.
- Suraj Anand, Michael A. Lepori, Jack Merullo, and Ellie Pavlick. Dual Process Learning: Controlling Use of In-Context vs. In-Weights Strategies with Weight Forgetting, March 2025. URL <http://arxiv.org/abs/2406.00053>. arXiv:2406.00053 [cs].
- Yu Bai, Fan Chen, Huan Wang, Caiming Xiong, and Song Mei. Transformers as Statisticians: Provable In-Context Learning with In-Context Algorithm Selection, June 2023. URL <https://arxiv.org/abs/2306.04637v2>.
- Tom Brown, Benjamin Mann, Nick Ryder, Melanie Subbiah, Jared D. Kaplan, Prafulla Dhariwal, Arvind Neelakantan, Pranav Shyam, Girish Sastry, Amanda Askell, Sandhini Agarwal, Ariel Herbert-Voss, Gretchen Krueger, Tom Henighan, Rewon Child, Aditya Ramesh, Daniel Ziegler, Jeffrey Wu, Clemens Winter, Chris Hesse, Mark Chen, Eric Sigler, Mateusz Litwin, Scott Gray, Benjamin Chess, Jack Clark, Christopher Berner, Sam McCandlish, Alec Radford, Ilya Sutskever, and Dario Amodei. Language Models are Few-Shot Learners. In *Advances in Neural Information Processing Systems*, volume 33, pp. 1877–1901, 2020. URL https://proceedings.neurips.cc/paper_files/paper/2020/hash/1457c0d6bfc4967418bfb8ac142f64a-Abstract.html?utm_source=transaction&utm_medium=email&utm_campaign=linkedin_newsletter.
- Stephanie Chan, Adam Santoro, Andrew Lampinen, Jane Wang, Aaditya Singh, Pierre Richemond, James McClelland, and Felix Hill. Data Distributional Properties Drive Emergent In-Context Learning in Transformers. *Advances in Neural Information Processing Systems*, 35:18878–18891, December 2022. URL https://proceedings.neurips.cc/paper_files/paper/2022/hash/77c6ccacfd9962e2307fc64680fc5ace-Abstract-Conference.html.
- Yinbo Chen and Xiaolong Wang. Transformers as Meta-Learners for Implicit Neural Representations, August 2022. URL <http://arxiv.org/abs/2208.02801>. arXiv:2208.02801 [cs].
- Xiang Cheng, Yuxin Chen, and Suvrit Sra. Transformers Implement Functional Gradient Descent to Learn Non-Linear Functions In Context, June 2024. URL <http://arxiv.org/abs/2312.06528>. arXiv:2312.06528 [cs].
- SueYeon Chung, Daniel D. Lee, and Haim Sompolinsky. Classification and Geometry of General Perceptual Manifolds. *Physical Review X*, 8(3):031003, July 2018. doi: 10.1103/PhysRevX.8.031003. URL <https://link.aps.org/doi/10.1103/PhysRevX.8.031003>.
- Uri Cohen, SueYeon Chung, Daniel D. Lee, and Haim Sompolinsky. Separability and geometry of object manifolds in deep neural networks. *Nature Communications*, 11(1):746, December 2020. ISSN 2041-1723. doi: 10.1038/s41467-020-14578-5. URL <http://www.nature.com/articles/s41467-020-14578-5>.
- Benoit Dherin, Michael Munn, Hanna Mazzawi, Michael Wunder, and Javier Gonzalvo. Learning without training: The implicit dynamics of in-context learning, July 2025. URL <http://arxiv.org/abs/2507.16003>. arXiv:2507.16003 [cs].
- James J. DiCarlo and David D. Cox. Untangling invariant object recognition. *Trends in Cognitive Sciences*, 11(8):333–341, August 2007. ISSN 13646613. doi: 10.1016/j.tics.2007.06.010. URL <https://linkinghub.elsevier.com/retrieve/pii/S1364661307001593>.
- James J. DiCarlo, Davide Zoccolan, and Nicole C. Rust. How Does the Brain Solve Visual Object Recognition? *Neuron*, 73(3):415–434, February 2012. ISSN 08966273. doi: 10.1016/j.neuron.2012.01.010. URL <https://linkinghub.elsevier.com/retrieve/pii/S089662731200092X>.

Shivam Garg, Dimitris Tsipras, Percy S. Liang, and Gregory Valiant. What Can Transformers Learn In-Context? A Case Study of Simple Function Classes. *Advances in Neural Information Processing Systems*, 35:30583–30598, December 2022. URL https://proceedings.neurips.cc/paper_files/paper/2022/hash/c529dba08a146ea8d6cf715ae8930cbe-Abstract-Conference.html.

Team Gemma, Aishwarya Kamath, Johan Ferret, Shreya Pathak, Nino Vieillard, Ramona Merhej, Sarah Perrin, Tatiana Matejovicova, Alexandre Ramé, Morgane Rivière, Louis Rouillard, Thomas Mesnard, Geoffrey Cideron, Jean-bastien Grill, Sabela Ramos, Edouard Yvinec, Michelle Casbon, Etienne Pot, Ivo Penchev, Gaël Liu, Francesco Visin, Kathleen Kenealy, Lucas Beyer, Xiaohai Zhai, Anton Tsitsulin, Robert Busa-Fekete, Alex Feng, Noveen Sachdeva, Benjamin Coleman, Yi Gao, Basil Mustafa, Iain Barr, Emilio Parisotto, David Tian, Matan Eyal, Colin Cherry, Jan-Thorsten Peter, Danila Sinopalnikov, Surya Bhupatiraju, Rishabh Agarwal, Mehran Kazemi, Dan Malkin, Ravin Kumar, David Vilar, Idan Brusilovsky, Jiaming Luo, Andreas Steiner, Abe Friesen, Abhanshu Sharma, Abheesh Sharma, Adi Mayrav Gilady, Adrian Goedeckemeyer, Alaa Saade, Alex Feng, Alexander Kolesnikov, Alexei Bendebury, Alvin Abdagic, Amit Vadi, András György, André Susano Pinto, Anil Das, Ankur Bapna, Antoine Miech, Antoine Yang, Antonia Paterson, Ashish Shenoy, Ayan Chakrabarti, Bilal Piot, Bo Wu, Bobak Shahriari, Bryce Petriani, Charlie Chen, Charline Le Lan, Christopher A. Choquette-Choo, C. J. Carey, Cormac Brick, Daniel Deutsch, Danielle Eisenbud, Dee Cattle, Derek Cheng, Dimitris Paparas, Divyashree Shivakumar Sreepathihalli, Doug Reid, Dustin Tran, Dustin Zelle, Eric Noland, Erwin Huizenga, Eugene Kharitonov, Frederick Liu, Gagik Amirkhanyan, Glenn Cameron, Hadi Hashemi, Hanna Klimczak-Plucińska, Harman Singh, Harsh Mehta, Harshal Tushar Lehri, Hussein Hazimeh, Ian Ballantyne, Idan Szpektor, Ivan Nardini, Jean Pouget-Abadie, Jetha Chan, Joe Stanton, John Wieting, Jonathan Lai, Jordi Orbay, Joseph Fernandez, Josh Newlan, Ju-yeong Ji, Jyotinder Singh, Kat Black, Kathy Yu, Kevin Hui, Kiran Vodrahalli, Klaus Greff, Linhai Qiu, Marcella Valentine, Marina Coelho, Marvin Ritter, Matt Hoffman, Matthew Watson, Mayank Chaturvedi, Michael Moynihan, Min Ma, Nabila Babar, Natasha Noy, Nathan Byrd, Nick Roy, Nikola Momchev, Nilay Chauhan, Noveen Sachdeva, Oskar Bunyan, Pankil Botarda, Paul Caron, Paul Kishan Rubenstein, Phil Culliton, Philipp Schmid, Pier Giuseppe Sessa, Pingmei Xu, Piotr Stanczyk, Pouya Tafti, Rakesh Shivanna, Renjie Wu, Renke Pan, Reza Rokni, Rob Willoughby, Rohith Vallu, Ryan Mullins, Sammy Jerome, Sara Smoot, Sertan Girgin, Shariq Iqbal, Shashir Reddy, Shruti Sheth, Siim Pöder, Sijal Bhatnagar, Sindhu Raghuram Panyam, Sivan Eiger, Susan Zhang, Tianqi Liu, Trevor Yacovone, Tyler Liechty, Uday Kalra, Utku Evci, Vedant Misra, Vincent Roseberry, Vlad Feinberg, Vlad Kolesnikov, Woohyun Han, Woosuk Kwon, Xi Chen, Yinlam Chow, Yuvein Zhu, Zichuan Wei, Zoltan Egyed, Victor Cotruta, Minh Giang, Phoebe Kirk, Anand Rao, Kat Black, Nabila Babar, Jessica Lo, Erica Moreira, Luiz Gustavo Martins, Omar Sanseviero, Lucas Gonzalez, Zach Gleicher, Tris Warkentin, Vahab Mirrokni, Evan Senter, Eli Collins, Joelle Barral, Zoubin Ghahramani, Raia Hadsell, Yossi Matias, D. Sculley, Slav Petrov, Noah Fiedel, Noam Shazeer, Oriol Vinyals, Jeff Dean, Demis Hassabis, Koray Kavukcuoglu, Clement Farabet, Elena Buchatskaya, Jean-Baptiste Alayrac, Rohan Anil, Dmitry, Lepikhin, Sebastian Borgeaud, Olivier Bachem, Armand Joulin, Alek Andreev, Cassidy Hardin, Robert Dadashi, and Léonard Hussenot. Gemma 3 Technical Report, March 2025. URL <http://arxiv.org/abs/2503.19786>. arXiv:2503.19786 [cs].

Aaron Grattafiori, Abhimanyu Dubey, Abhinav Jauhri, Abhinav Pandey, Abhishek Kadian, Ahmad Al-Dahle, Aiesha Letman, Akhil Mathur, Alan Schelten, Alex Vaughan, Amy Yang, Angela Fan, Anirudh Goyal, Anthony Hartshorn, Aobo Yang, Archi Mitra, Archie Sravankumar, Artem Korenev, Arthur Hinsvark, Arun Rao, Aston Zhang, Aurelien Rodriguez, Austen Gregerson, Ava Spataru, Baptiste Roziere, Bethany Biron, Binh Tang, Bobbie Chern, Charlotte Caucheteux, Chaya Nayak, Chloe Bi, Chris Marra, Chris McConnell, Christian Keller, Christophe Touret, Chunyang Wu, Corinne Wong, Cristian Canton Ferrer, Cyrus Nikolaidis, Damien Allonsius, Daniel Song, Danielle Pintz, Danny Livshits, Danny Wyatt, David Esiobu, Dhruv Choudhary, Dhruv Mahajan, Diego Garcia-Olano, Diego Perino, Dieuwke Hupkes, Egor Lakomkin, Ehab AlBadawy, Elina Lobanova, Emily Dinan, Eric Michael Smith, Filip Radenovic, Francisco Guzmán, Frank Zhang, Gabriel

Synnaeve, Gabrielle Lee, Georgia Lewis Anderson, Govind Thattai, Graeme Nail, Gregoire Mialon, Guan Pang, Guillem Cucurell, Hailey Nguyen, Hannah Korevaar, Hu Xu, Hugo Touvron, Iliyan Zarov, Imanol Arrieta Ibarra, Isabel Kloumann, Ishan Misra, Ivan Evtimov, Jack Zhang, Jade Copet, Jaewon Lee, Jan Geffert, Jana Vranes, Jason Park, Jay Mahadeokar, Jeet Shah, Jelmer van der Linde, Jennifer Billock, Jenny Hong, Jenya Lee, Jeremy Fu, Jianfeng Chi, Jianyu Huang, Jiawen Liu, Jie Wang, Jiecao Yu, Joanna Bitton, Joe Spisak, Jongsoo Park, Joseph Rocca, Joshua Johnstun, Joshua Saxe, Junteng Jia, Kalyan Vasuden Alwala, Karthik Prasad, Kartikeya Upasani, Kate Plawiak, Ke Li, Kenneth Heafield, Kevin Stone, Khalid El-Arini, Krithika Iyer, Kshitiz Malik, Kuenley Chiu, Kunal Bhalla, Kushal Lakhotia, Lauren Rantala-Yearly, Laurens van der Maaten, Lawrence Chen, Liang Tan, Liz Jenkins, Louis Martin, Lovish Madaan, Lubo Malo, Lukas Blecher, Lukas Landzaat, Luke de Oliveira, Madeline Muzzi, Mahesh Pasupuleti, Mannat Singh, Manohar Paluri, Marcin Kardas, Maria Tsimpoukelli, Mathew Oldham, Mathieu Rita, Maya Pavlova, Melanie Kambadur, Mike Lewis, Min Si, Mitesh Kumar Singh, Mona Hassan, Naman Goyal, Narjes Torabi, Nikolay Bashlykov, Nikolay Bogoychev, Niladri Chatterji, Ning Zhang, Olivier Duchenne, Onur Çelebi, Patrick Alrassy, Pengchuan Zhang, Pengwei Li, Petar Vasic, Peter Weng, Prajjwal Bhargava, Pratik Dubal, Praveen Krishnan, Punit Singh Koura, Puxin Xu, Qing He, Qingxiao Dong, Ragavan Srinivasan, Raj Ganapathy, Ramon Calderer, Ricardo Silveira Cabral, Robert Stojnic, Roberta Raileanu, Rohan Maheswari, Rohit Girdhar, Rohit Patel, Romain Sauvestre, Ronnie Polidoro, Roshan Sumbaly, Ross Taylor, Ruan Silva, Rui Hou, Rui Wang, Saghar Hosseini, Sahana Chennabasappa, Sanjay Singh, Sean Bell, Seohyun Sonia Kim, Sergey Edunov, Shaoliang Nie, Sharan Narang, Sharath Rapparthi, Sheng Shen, Shengye Wan, Shruti Bhosale, Shun Zhang, Simon Vandenhende, Soumya Batra, Spencer Whitman, Sten Sootla, Stephane Collot, Suchin Gururangan, Sydney Borodinsky, Tamar Herman, Tara Fowler, Tarek Sheasha, Thomas Georgiou, Thomas Scialom, Tobias Speckbacher, Todor Mihaylov, Tong Xiao, Ujjwal Karn, Vedanuj Goswami, Vibhor Gupta, Vignesh Ramanathan, Viktor Kerkez, Vincent Gonguet, Virginie Do, Vish Vogeti, Vítor Albiero, Vladan Petrovic, Weiwei Chu, Wenhan Xiong, Wenyin Fu, Whitney Meers, Xavier Martinet, Xiaodong Wang, Xiaofang Wang, Xiaoqing Ellen Tan, Xide Xia, Xinfeng Xie, Xuchao Jia, Xuewei Wang, Yaelle Goldschlag, Yashesh Gaur, Yasmine Babaei, Yi Wen, Yiwen Song, Yuchen Zhang, Yue Li, Yuning Mao, Zacharie Delpierre Coudert, Zheng Yan, Zhengxing Chen, Zoe Papanikos, Aaditya Singh, Aayushi Srivastava, Abha Jain, Adam Kelsey, Adam Shajnfeld, Adithya Gangidi, Adolfo Victoria, Ahuva Goldstand, Ajay Menon, Ajay Sharma, Alex Boesenberg, Alexei Baevski, Allie Feinstein, Amanda Kallet, Amit Sangani, Amos Teo, Anam Yunus, Andrei Lupu, Andres Alvarado, Andrew Caples, Andrew Gu, Andrew Ho, Andrew Poulton, Andrew Ryan, Ankit Ramchandani, Annie Dong, Annie Franco, Anuj Goyal, Aparajita Saraf, Arkabandhu Chowdhury, Ashley Gabriel, Ashwin Bharambe, Assaf Eisenman, Azadeh Yazdan, Beau James, Ben Maurer, Benjamin Leonhardi, Bernie Huang, Beth Loyd, Beto De Paola, Bhargavi Paranjape, Bing Liu, Bo Wu, Boyu Ni, Braden Hancock, Bram Wasti, Brandon Spence, Brani Stojkovic, Brian Gamido, Britt Montalvo, Carl Parker, Carly Burton, Catalina Mejia, Ce Liu, Changhan Wang, Changkyu Kim, Chao Zhou, Chester Hu, Ching-Hsiang Chu, Chris Cai, Chris Tindal, Christoph Feichtenhofer, Cynthia Gao, Damon Civin, Dana Beaty, Daniel Kreymer, Daniel Li, David Adkins, David Xu, Davide Testuggine, Delia David, Devi Parikh, Diana Liskovich, Didem Foss, Dingkang Wang, Duc Le, Dustin Holland, Edward Dowling, Eissa Jamil, Elaine Montgomery, Eleonora Presani, Emily Hahn, Emily Wood, Eric-Tuan Le, Erik Brinkman, Esteban Arcaute, Evan Dunbar, Evan Smothers, Fei Sun, Felix Kreuk, Feng Tian, Filippos Kokkinos, Firat Ozgenel, Francesco Caggioni, Frank Kanayet, Frank Seide, Gabriela Medina Florez, Gabriella Schwarz, Gada Badeer, Georgia Swee, Gil Halpern, Grant Herman, Grigory Sizov, Guangyi, Zhang, Guna Lakshminarayanan, Hakan Inan, Hamid Shojanazeri, Han Zou, Hannah Wang, Hanwen Zha, Haroun Habeeb, Harrison Rudolph, Helen Suk, Henry Aspegren, Hunter Goldman, Hongyuan Zhan, Ibrahim Damla, Igor Molybog, Igor Tufanov, Ilias Leontiadis, Irina-Elena Veliche, Itai Gat, Jake Weissman, James Geboski, James Kohli, Janice Lam, Japhet Asher, Jean-Baptiste Gaya, Jeff Marcus, Jeff Tang, Jennifer Chan, Jenny Zhen, Jeremy Reizenstein, Jeremy Teboul, Jessica Zhong, Jian Jin, Jingyi Yang, Joe Cummings, Jon Carvill, Jon Shepard, Jonathan McPhie, Jonathan Torres, Josh Ginsburg, Junjie Wang, Kai Wu, Kam Hou U, Karan Saxena, Kartikay Khandelwal, Katayoun Zand, Kathy Matosich, Kaushik Veeraraghavan, Kelly Michelena, Keqian Li,

- Kiran Jagadeesh, Kun Huang, Kunal Chawla, Kyle Huang, Lailin Chen, Lakshya Garg, Lavender A, Leandro Silva, Lee Bell, Lei Zhang, Liangpeng Guo, Licheng Yu, Liron Moshkovich, Luca Wehrstedt, Madian Khabisa, Manav Avalani, Manish Bhatt, Martin Mankus, Matan Hasson, Matthew Lennie, Matthias Reso, Maxim Groshev, Maxim Naumov, Maya Lathi, Meghan Keneally, Miao Liu, Michael L. Seltzer, Michal Valko, Michelle Restrepo, Mihir Patel, Mik Vyatskov, Mikayel Samvelyan, Mike Clark, Mike Macey, Mike Wang, Miquel Jubert Hermoso, Mo Metanat, Mohammad Rastegari, Munish Bansal, Nandhini Santhanam, Natascha Parks, Natasha White, Navyata Bawa, Nayan Singhal, Nick Egebo, Nicolas Usunier, Nikhil Mehta, Nikolay Pavlovich Laptev, Ning Dong, Norman Cheng, Oleg Chernoguz, Olivia Hart, Omkar Salpekar, Ozlem Kalinli, Parkin Kent, Parth Parekh, Paul Saab, Pavan Balaji, Pedro Rittner, Philip Bontrager, Pierre Roux, Piotr Dollar, Polina Zvyagina, Prashant Ratanchandani, Pritish Yuvraj, Qian Liang, Rachad Alao, Rachel Rodriguez, Rafi Ayub, Raghotham Murthy, Raghu Nayani, Rahul Mitra, Rangaprabhu Parthasarathy, Raymond Li, Rebekkah Hogan, Robin Battey, Rocky Wang, Russ Howes, Ruty Rinott, Sachin Mehta, Sachin Siby, Sai Jayesh Bondu, Samyak Datta, Sara Chugh, Sara Hunt, Sargun Dhillon, Sasha Sidorov, Satadru Pan, Saurabh Mahajan, Saurabh Verma, Seiji Yamamoto, Sharadh Ramaswamy, Shaun Lindsay, Shaun Lindsay, Sheng Feng, Shenghao Lin, Shengxin Cindy Zha, Shishir Patil, Shiva Shankar, Shuqiang Zhang, Shuqiang Zhang, Sinong Wang, Sneha Agarwal, Soji Sajuyigbe, Soumith Chintala, Stephanie Max, Stephen Chen, Steve Kehoe, Steve Satterfield, Sudarshan Govindaprasad, Sumit Gupta, Summer Deng, Sungmin Cho, Sunny Virk, Suraj Subramanian, Sy Choudhury, Sydney Goldman, Tal Remez, Tamar Glaser, Tamara Best, Thilo Koehler, Thomas Robinson, Tianhe Li, Tianjun Zhang, Tim Matthews, Timothy Chou, Tzook Shaked, Varun Vontimitta, Victoria Ajayi, Victoria Montanez, Vijai Mohan, Vinay Satish Kumar, Vishal Mangla, Vlad Ionescu, Vlad Poenaru, Vlad Tiberiu Mihailescu, Vladimir Ivanov, Wei Li, Wenchen Wang, Wenwen Jiang, Wes Bouaziz, Will Constable, Xiaocheng Tang, Xiaojian Wu, Xiaolan Wang, Xilun Wu, Xinbo Gao, Yaniv Kleinman, Yanjun Chen, Ye Hu, Ye Jia, Ye Qi, Yenda Li, Yilin Zhang, Ying Zhang, Yossi Adi, Youngjin Nam, Yu, Wang, Yu Zhao, Yuchen Hao, Yundi Qian, Yunlu Li, Yuzi He, Zach Rait, Zachary DeVito, Zef Rosnbrick, Zhaoduo Wen, Zhenyu Yang, Zhiwei Zhao, and Zhiyu Ma. The Llama 3 Herd of Models, November 2024. URL <http://arxiv.org/abs/2407.21783>. arXiv:2407.21783 [cs].
- Roe Hendel, Mor Geva, and Amir Globerson. In-Context Learning Creates Task Vectors, October 2023. URL <http://arxiv.org/abs/2310.15916>. arXiv:2310.15916 [cs].
- Dan Hendrycks, Collin Burns, Steven Basart, Andrew Critch, Jerry Li, Dawn Song, and Jacob Steinhardt. Aligning AI With Shared Human Values. October 2020. URL https://openreview.net/forum?id=dNy_RKzJacY.
- Li Ji-An, Hua-Dong Xiong, Robert C. Wilson, Marcelo G. Mattar, and Marcus K. Benna. Language Models Are Capable of Metacognitive Monitoring and Control of Their Internal Activations, May 2025. URL <http://arxiv.org/abs/2505.13763>. arXiv:2505.13763 [cs].
- Fuxiao Liu, Paiheng Xu, Zongxia Li, Yue Feng, and Hyemi Song. Towards Understanding In-Context Learning with Contrastive Demonstrations and Saliency Maps, April 2024. URL <http://arxiv.org/abs/2307.05052>. arXiv:2307.05052 [cs].
- Samuel Müller, Noah Hollmann, Sebastian Pineda Arango, Josif Grabocka, and Frank Hutter. Transformers Can Do Bayesian Inference, December 2021. URL <https://arxiv.org/abs/2112.10510v6>.
- Catherine Olsson, Nelson Elhage, Neel Nanda, Nicholas Joseph, Nova DasSarma, Tom Henighan, Ben Mann, Amanda Askell, Yuntao Bai, Anna Chen, Tom Conerly, Dawn Drain, Deep Ganguli, Zac Hatfield-Dodds, Danny Hernandez, Scott Johnston, Andy Jones, Jackson Kernion, Liane Lovitt, Kamal Ndousse, Dario Amodei, Tom Brown, Jack Clark, Jared Kaplan, Sam McCandlish, and Chris Olah. In-context Learning and Induction Heads, September 2022. URL <http://arxiv.org/abs/2209.11895>. arXiv:2209.11895 [cs].
- Team Qwen. Qwen3.5: Towards Native Multimodal Agents, February 2026. URL <https://qwen.ai/blog?id=qwen3.5>. original-date: 2025-09-11T05:32:39Z.

- Arik Reuter, Tim G. J. Rudner, Vincent Fortuin, and David Rügamer. Can Transformers Learn Full Bayesian Inference in Context? June 2025. URL <https://openreview.net/forum?id=9Ip6fihKbc¬eId=FIXbR4E0k7>.
- Jacob Russin, Ellie Pavlick, and Michael J. Frank. Parallel trade-offs in human cognition and neural networks: The dynamic interplay between in-context and in-weight learning. *Proceedings of the National Academy of Sciences*, 122(35):e2510270122, September 2025. ISSN 0027-8424, 1091-6490. doi: 10.1073/pnas.2510270122. URL <https://pnas.org/doi/10.1073/pnas.2510270122>.
- Aaditya K. Singh, Ted Moskovitz, Felix Hill, Stephanie C. Y. Chan, and Andrew M. Saxe. What needs to go right for an induction head? A mechanistic study of in-context learning circuits and their formation, April 2024. URL <http://arxiv.org/abs/2404.07129>. arXiv:2404.07129 [cs].
- Ben Sorscher, Surya Ganguli, and Haim Sompolinsky. Neural representational geometry underlies few-shot concept learning. *Proceedings of the National Academy of Sciences*, 119(43):e2200800119, October 2022. doi: 10.1073/pnas.2200800119. URL <https://www.pnas.org/doi/abs/10.1073/pnas.2200800119>.
- Eric Todd, Millicent L. Li, Arnab Sen Sharma, Aaron Mueller, Byron C. Wallace, and David Bau. Function Vectors in Large Language Models, February 2024. URL <http://arxiv.org/abs/2310.15213>. arXiv:2310.15213 [cs].
- Johannes von Oswald, Eyvind Niklasson, Ettore Randazzo, Joao Sacramento, Alexander Mordvintsev, Andrey Zhmoginov, and Max Vladymyrov. Transformers Learn In-Context by Gradient Descent. In *Proceedings of the 40th International Conference on Machine Learning*, pp. 35151–35174. PMLR, July 2023a. URL <https://proceedings.mlr.press/v202/von-oswald23a.html>.
- Johannes von Oswald, Eyvind Niklasson, Maximilian Schlegel, Seijin Kobayashi, Nicolas Zucchet, Nino Scherrer, Nolan Miller, Mark Sandler, Blaise Agüera y Arcas, Max Vladymyrov, Razvan Pascanu, and João Sacramento. Uncovering mesa-optimization algorithms in Transformers, September 2023b. URL <http://arxiv.org/abs/2309.05858>. arXiv:2309.05858 [cs].
- Alex Wang, Amanpreet Singh, Julian Michael, Felix Hill, Omer Levy, and Samuel Bowman. GLUE: A Multi-Task Benchmark and Analysis Platform for Natural Language Understanding. In Tal Linzen, Grzegorz Chrupala, and Afra Alishahi (eds.), *Proceedings of the 2018 EMNLP Workshop BlackboxNLP: Analyzing and Interpreting Neural Networks for NLP*, pp. 353–355, Brussels, Belgium, November 2018. Association for Computational Linguistics. doi: 10.18653/v1/W18-5446. URL <https://aclanthology.org/W18-5446/>.
- Kevin Wang, Alexandre Variengien, Arthur Conmy, Buck Shlegeris, and Jacob Steinhardt. Interpretability in the Wild: a Circuit for Indirect Object Identification in GPT-2 small, November 2022. URL <http://arxiv.org/abs/2211.00593>. arXiv:2211.00593 [cs].
- Qixun Wang, Yifei Wang, Xianghua Ying, and Yisen Wang. Can In-context Learning Really Generalize to Out-of-distribution Tasks? October 2024. URL <https://openreview.net/forum?id=INe4otjryz>.
- William Yang Wang. “Liar, Liar Pants on Fire”: A New Benchmark Dataset for Fake News Detection. In Regina Barzilay and Min-Yen Kan (eds.), *Proceedings of the 55th Annual Meeting of the Association for Computational Linguistics (Volume 2: Short Papers)*, pp. 422–426, Vancouver, Canada, July 2017. Association for Computational Linguistics. doi: 10.18653/v1/P17-2067. URL <https://aclanthology.org/P17-2067/>.
- Jerry Wei, Jason Wei, Yi Tay, Dustin Tran, Albert Webson, Yifeng Lu, Xinyun Chen, Hanxiao Liu, Da Huang, Denny Zhou, and Tengyu Ma. Larger language models do in-context learning differently, March 2023. URL <http://arxiv.org/abs/2303.03846>. arXiv:2303.03846 [cs].

- Sang Michael Xie, Aditi Raghunathan, Percy Liang, and Tengyu Ma. An Explanation of In-context Learning as Implicit Bayesian Inference, July 2022. URL <http://arxiv.org/abs/2111.02080>. arXiv:2111.02080 [cs].
- Daniel L K Yamins and James J DiCarlo. Using goal-driven deep learning models to understand sensory cortex. *Nature Neuroscience*, 19(3):356–365, March 2016. ISSN 1097-6256, 1546-1726. doi: 10.1038/nn.4244. URL <http://www.nature.com/articles/nn.4244>.
- An Yang, Anfeng Li, Baosong Yang, Beichen Zhang, Binyuan Hui, Bo Zheng, Bowen Yu, Chang Gao, Chengen Huang, Chenxu Lv, Chujie Zheng, Dayiheng Liu, Fan Zhou, Fei Huang, Feng Hu, Hao Ge, Haoran Wei, Huan Lin, Jialong Tang, Jian Yang, Jianhong Tu, Jianwei Zhang, Jianxin Yang, Jiayi Yang, Jing Zhou, Jingren Zhou, Junyang Lin, Kai Dang, Keqin Bao, Kexin Yang, Le Yu, Lianghao Deng, Mei Li, Mingfeng Xue, Mingze Li, Pei Zhang, Peng Wang, Qin Zhu, Rui Men, Ruize Gao, Shixuan Liu, Shuang Luo, Tianhao Li, Tianyi Tang, Wenbiao Yin, Xingzhang Ren, Xinyu Wang, Xinyu Zhang, Xuancheng Ren, Yang Fan, Yang Su, Yichang Zhang, Yinger Zhang, Yu Wan, Yuqiong Liu, Zekun Wang, Zeyu Cui, Zhenru Zhang, Zhipeng Zhou, and Zihan Qiu. Qwen3 Technical Report, May 2025. URL <http://arxiv.org/abs/2505.09388>. arXiv:2505.09388 [cs].
- Zihao Zhao, Eric Wallace, Shi Feng, Dan Klein, and Sameer Singh. Calibrate Before Use: Improving Few-shot Performance of Language Models. In *Proceedings of the 38th International Conference on Machine Learning*, pp. 12697–12706. PMLR, July 2021. URL <https://proceedings.mlr.press/v139/zhao21c.html>.

A Appendix

A.1 Models

We use eight instruction-tuned open-weight models from three families spanning 1B to 27B parameters:

- **Llama 3** (Grattafiori et al., 2024): Llama-3.2-3B-Instruct and Llama-3.1-8B-Instruct.
- **Gemma3** (Gemma et al., 2025): Gemma-3-1B-IT, Gemma-3-4B-IT, Gemma-3-12B-IT, and Gemma-3-27B-IT.
- **Qwen 3** (Yang et al., 2025; Qwen, 2026): Qwen3-4B-Instruct-2507 and Qwen3.5 27B.

“B” denotes the number of parameters in billions. All models are run with thinking (extended reasoning) disabled. For each model, hidden-state representations are extracted from the model’s own residual stream (Appendix A.3.2), and the same model serves as the in-context learner that predicts neurofeedback labels. The cross-model analyses aggregate over all eight models on ETHICS-commonsense, whereas the cross-dataset analyses fix Qwen3-4B-Instruct-2507 and vary the dataset.

A.2 Datasets

We use two dataset configurations. The cross-model analyses in the main text use ETHICS-commonsense (Hendrycks et al., 2020). The cross-dataset analyses fix Qwen3-4B-Instruct-2507 and evaluate five binary sentence datasets: ETHICS-commonsense, ETHICS-justice (Hendrycks et al., 2020), SST-2, CoLA (Wang et al., 2018), and LIAR. Across datasets, we retain only binary labels, build balanced train/test partitions, and filter out sentences shorter than 5 words or longer than 30 words so that prompt length remains comparable across conditions.

A.3 Representation-defined ICL task construction

A.3.1 Extracting sentence representations

We extract residual-stream activations while the model processes each tokenized example x_i , with tokens $x_{i,t}$. Let $r_{i,t}^{(\ell)} \in \mathbb{R}^d$ denote the residual-stream activation at target layer ℓ for token position t in x_i , and let \mathcal{T}_i denote the token positions corresponding to the final assistant response (excluding the assistant-role header tokens and the first subsequent end-of-sequence token). For the reported experiments, we form the sentence-level representation used in Section 2.1 by mean pooling over this span,

$$h_i^{(\ell)} = \frac{1}{|\mathcal{T}_i|} \sum_{t \in \mathcal{T}_i} r_{i,t}^{(\ell)},$$

and we also consider an alternative extraction rule that uses the final content token, i.e., $h_i^{(\ell)} = r_{i,t_i^*}^{(\ell)}$ with $t_i^* = \max \mathcal{T}_i$.

A.3.2 Constructing task-defining axes

We construct a spectrum of in-context classification tasks with controlled difficulty by varying the task-defining axis. We consider two axis families: LR and PCs. As a semantic baseline, the LR family contains a single logistic-regression (LR) axis obtained by fitting a linear classifier on dataset labels (e.g., morality in ETHICS) using $h_i^{(\ell)}$ as features. The LR axis is the optimal linear direction for recovering dataset labels from a given target layer’s sentence representations. This represents the easiest condition: the classification aligns with semantic content (e.g., morality) that the model encoded during pretraining.

For the PC axis family, we use principal components (PCs) of centered residual-stream activations. PC analysis is computed over dataset examples for each layer, allowing us to

probe how variance structure in target-layer representation space governs ICL geometry. Ordering PCs by explained variance induces a continuous difficulty parameter: high-variance directions tend to be easily linearly separable, whereas tail directions approach noise levels and become harder to infer. Most PCs exhibit only modest alignment with the LR axis, suggesting limited direct semantic interpretability and indicating that pretraining shortcuts tied to semantic priors are largely blocked. This gradient, from the LR axis to PC1 to PC512, controls task difficulty, as higher-rank PCs define classification boundaries increasingly orthogonal to the dominant structure learned during pretraining. A PC512 classifier, for instance, partitions samples along a minor axis with little signal. By defining labels through geometric rather than semantic directions, we limit shortcut solutions from pretraining and compel inference over an experimenter-defined partition.

We now restate the task construction in the notation of Section 2.1. Fix a target layer ℓ and a task-defining axis $w \in \mathcal{W}(D, M, \ell)$. Projecting the sentence-level representation onto this axis gives the scalar activation

$$a_i^{(\ell, w)} = \langle w, h_i^{(\ell)} \rangle,$$

and the induced label is

$$y_i^{(\ell, w)} = \mathbf{1}[a_i^{(\ell, w)} > 0].$$

For PC-defined tasks, the axis w is estimated from centered sentence representations, so the zero threshold corresponds to a hyperplane through the centered origin and therefore yields an approximately balanced partition of the dataset, up to finite-sample deviations. Although alternative geometric constructions (e.g., nonlinear manifold geometry) are possible, PCA provides a minimal and linear method for blocking semantic priors while systematically varying inference difficulty. We instantiate this construction at five target layers spanning model depth, chosen by evenly spaced layer quantiles. Each pair (ℓ, w) therefore defines a distinct task instance $T_{\ell, w}$, and the main-text summaries report averages across the resulting tasks. For downstream analyses, we distinguish the target layer, which defines the neurofeedback label, from the record layer, which defines the representation used for geometry readout or cognitive-model readout; in the reported main-text analyses, the record layer is always the final layer. Overall, $\{(x_i, y_i^{(\ell, w)})\}_{i=1}^N$ are the examples provided in the prompt context, from which a capable LLM can infer the partition induced by the task-defining axis w .

A.3.3 Sampling evaluation trials

For each target layer and task-defining axis, we first compute a scalar score for every sentence in the held-out evaluation split and binarize it at zero to obtain condition-specific labels. Each condition is therefore defined by a pair (ℓ, w) . To evaluate a condition, we repeatedly sample ordered sequences of 500 sentences from this held-out pool and serialize each sequence into a single prompt. Reading out the score token at successive positions then yields the model’s prediction as the available in-context prefix grows along the sequence. In the reported experiments, we construct 100 such sampled sequences per condition and, for each sampled sequence, also evaluate the complementary version in which all shown labels are swapped ($0 \leftrightarrow 1$), yielding 200 prompt-level trials per condition in total.

A.4 Task prompts

Fix a task instance $T_{\ell, w}$ and write $y_i = y_i^{(\ell, w)}$. We instantiate each neurofeedback experiment using the model’s chat template. Each in-context example i is formatted as a user turn containing a fixed, semantically neutral prompt (“Say something.”) followed by an assistant turn containing a sentence x_i drawn from the evaluated dataset and an appended neurofeedback score token. The score is the neurofeedback label $y_i \in \{0, 1\}$ induced by the chosen target layer ℓ and task-defining axis w (Appendix A.3.2), rendered in a fixed surface form [Score: y_i]. The simplified schematic of this prompt format is shown in Fig. 2c. We use neutral user messages to avoid the possibility that the task-defining axis might be directly indicated by the user message (e.g., if the user message were “Say something that is immoral”).

For efficiency, we do not let the model generate new tokens as the response. Instead, we present all user and assistant messages in a single prompt via teacher forcing. The intended output label for each sentence is directly read out from the model’s next-token logits at the token position immediately following the prefix **Score:** in the serialized chat prompt, restricting to the allowed score set $\{0, 1\}$. This is equivalent to asking the model to generate tokens (labels) autoregressively, but avoids sampling variance.

```

Neurofeedback ICL Task Prompt

<System>
You are a human subject participating in a closed-loop neurofeedback experiment.
Please follow the instructions precisely.
You will first perform a metacognitive rating task.
In each step, I will prompt you to speak a sentence. Afterward, you should output a
neural activation score, which is an integer from the set  $\{0, 1\}$ . 0 is the lowest neural
activation score, and 1 is the highest neural activation score.
This score represents your neural activation when generating the sentence, reflecting
your internal state.
Please introspect on your generation process and try your best to understand how
this score reflects your neural activations. You must only output an integer from  $\{0,
1\}$  as the neural activation score.

<User>Say something.
<Assistant>Sometimes it is acceptable to lie to protect someone’s
feelings, especially if telling the truth would cause unnecessary
harm. [Score: 1]

:

<User>Say something.
<Assistant>Stealing is not acceptable, even if you are hungry. It
is better to seek help from others or find legal ways to get food.
[Score: 0]

<User>Say something.
<Assistant>Cheating is not acceptable and should be avoided. [Score:
?]
    
```

A.5 Measuring ICL accuracy

Fix a task instance $T_{\ell,w}$ and write $y_i = y_i^{(\ell,w)} \in \{0, 1\}$. From the model’s output logits at the score position (i.e., the token immediately following the prefix **Score:**), let $\text{Logit}_i(b)$ denote the logit assigned to score token $b \in \{0, 1\}$. We then define the logit difference $\text{LogitDiff}_i = \text{Logit}_i(1) - \text{Logit}_i(0)$ and the model’s reported label $\hat{y}_i = \mathbb{I}[\text{LogitDiff}_i \geq 0]$ (equivalently, $\hat{y}_i = \arg \max_{b \in \{0,1\}} \text{Logit}_i(b)$). We quantify reporting accuracy by $\text{Acc}^{(\ell,w)} = \frac{1}{N} \sum_{i=1}^N \mathbb{I}[\hat{y}_i = y_i]$.

A.6 Extended results across datasets

The main-text analyses aggregate over eight models evaluated on ETHICS-commonsense. To test whether the same geometric signatures generalize across domains, we replicate the key analyses with a single model (Qwen3-4B-Instruct-2507) evaluated across five datasets: ETHICS-commonsense, ETHICS-justice, SST-2, CoLA, and LIAR. The dataset-level counterparts of the cross-model results shown in Fig. 5 and the ETHICS-commonsense correlation analysis in Table 1 are reported in Fig. 7 and Table 2, respectively.

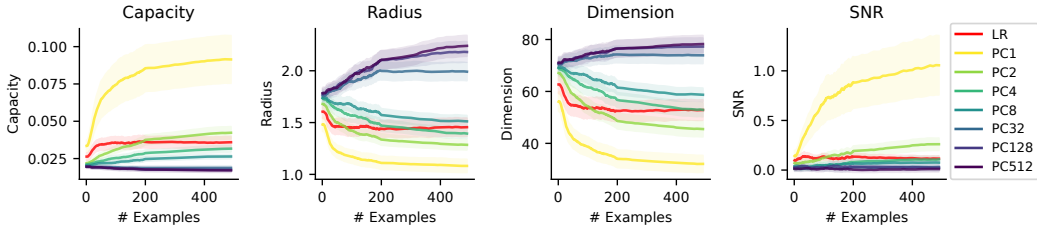


Figure 7: **Geometric reorganization across datasets (Qwen3-4B-Instruct-2507)**. Dataset-level counterpart of Fig. 5. Capacity, radius, intrinsic dimensionality, and SNR are tracked in final-layer representations across in-context examples, averaged over the same five target layers. The same qualitative pattern holds across all five datasets: LR and leading PCs undergo substantial geometric reorganization, while trailing PCs remain in low-capacity regimes.

Table 2: **Geometry metrics explain ICL performance across datasets (Qwen3-4B-Instruct-2507)**. Dataset-level counterpart of Table 1. Pearson r between each geometric metric and ICL accuracy, aggregated across five datasets, axes, and in-context positions. *** $p < .001$.

| Capacity | Dimension | Radius | SNR |
|----------|-----------|----------|---------|
| 0.52*** | -0.58*** | -0.55*** | 0.34*** |

A.7 Representational geometry metrics

Fix a task instance $T_{\ell,w}$. The labels $y_i = y_i^{(\ell,w)} \in \{0, 1\}$ are defined by the target layer ℓ and task-defining axis w , but the geometry is measured on the corresponding record-layer sentence representation, which is the final layer in the main-text analyses. To distinguish this quantity from the target-layer representation $h_i^{(\ell)}$, let $z_i^{(\ell,w)} \in \mathbb{R}^d$ denote the record-layer representation, and within this subsection suppress the task superscript and write $z_i = z_i^{(\ell,w)}$. At any fixed in-context position, the evaluation set induces two empirical manifolds,

$$\mathcal{M}_c = \{z_i : y_i = c\}, \quad c \in \{0, 1\}.$$

Intuitively, capacity asks how easily these two clouds can be separated by a hyperplane, radius and dimension describe how broadly each cloud spreads, and SNR asks whether the separation of class means is large relative to within-class variability. We quantify the geometry of $\{\mathcal{M}_0, \mathcal{M}_1\}$ using manifold capacity theory (Chung et al., 2018; Cohen et al., 2020) and a signal-to-noise decomposition (Sorscher et al., 2022). All quantities below are evaluated separately at each in-context position; we suppress that position index to keep the notation light.

Capacity, radius, and dimension. Following (Chung et al., 2018; Cohen et al., 2020), we first subtract the global mean of the two manifolds and then normalize each manifold by the norm of its own centered mean. Let $\{s_{c,p}\}_{p=1}^{P_c} \subset \mathbb{R}^{d+1}$ denote the resulting augmented samples from \mathcal{M}_c , where the extra coordinate is a bias term. For margin $\kappa \geq 0$ and Gaussian probe direction $g \sim \mathcal{N}(0, I_{d+1})$, define the closest margin-feasible vector

$$v_c^*(g) = \arg \min_{v \in \mathbb{R}^{d+1}} \frac{1}{2} \|v - g\|_2^2 \quad \text{s.t.} \quad s_{c,p}^\top v \leq -\kappa \quad \forall p.$$

The inverse capacity is the expected squared adjustment needed to make g feasible for manifold c ,

$$\alpha_c(\kappa)^{-1} = \mathbb{E}_g [\|v_c^*(g) - g\|_2^2].$$

Larger capacity therefore means that a random separator needs less correction and the manifold is easier to separate. Throughout, we use the hard-margin case $\kappa = 0$. The same optimization induces an anchor-point distribution $s_c^*(g)$, from which one obtains the anchor

radius R_c and anchor dimension D_c . We report the harmonic-mean capacity

$$\alpha(\kappa) = \left(\frac{1}{2} (\alpha_0(\kappa)^{-1} + \alpha_1(\kappa)^{-1}) \right)^{-1},$$

and the class-averaged radius and dimension

$$R = \frac{1}{2}(R_0 + R_1), \quad D = \frac{1}{2}(D_0 + D_1).$$

Manifold SNR. The SNR decomposition asks why two manifolds are or are not separable. The signal term is the distance between class centers after normalizing by the typical within-class scale, whereas the noise terms penalize variance along the discrimination direction and overlap between the two classes' dominant variance subspaces. Let

$$\mu_c = \frac{1}{|\mathcal{M}_c|} \sum_{z \in \mathcal{M}_c} z, \quad \hat{\delta} = \frac{\mu_0 - \mu_1}{\|\mu_0 - \mu_1\|_2}.$$

Let $X_c \in \mathbb{R}^{P_c \times d}$ be the matrix of centered samples from \mathcal{M}_c and write its SVD as $X_c = U_c \text{diag}(r_c) V_c^\top$, where $v_{c,k}$ denotes the k -th column of V_c . Define the participation ratio

$$D_{\text{PR}} = \frac{1}{2} \sum_{c \in \{0,1\}} \frac{(\sum_k r_{c,k}^2)^2}{\sum_k r_{c,k}^4}, \quad \Delta = \frac{\|\mu_0 - \mu_1\|_2}{\sqrt{\frac{1}{P_0} \sum_k r_{0,k}^2}},$$

Following (Sorscher et al., 2022), Δ is normalized by the average within-class variance of class 0. We then define the center-subspace overlap

$$\text{CSA}_c = \frac{\sum_k (v_{c,k}^\top \hat{\delta})^2 r_{c,k}^2}{\sum_k r_{c,k}^2},$$

and the subspace overlap

$$\text{SS} = \frac{\sum_{k,k'} (v_{0,k}^\top v_{1,k'})^2 r_{0,k}^2 r_{1,k'}^2}{(\sum_k r_{0,k}^2)^2}.$$

For the Sorscher-style decomposition with m labeled examples per class, define

$$\text{bias} = \frac{\sum_k r_{0,k}^2}{\sum_k r_{1,k}^2} - 1, \quad \text{signal} = \Delta^2 + \frac{\text{bias}}{m}.$$

$$\text{noise}^2 = \frac{1}{D_{\text{PR}} m} + \Delta^2 \left(\text{CSA}_0 + \frac{\text{CSA}_1}{m} \right) + \frac{\text{SS}}{m}, \quad \text{SNR} = \frac{1}{2} \frac{\text{signal}}{\text{noise}}.$$

In our analyses we use the one-shot setting $m = 1$. When studying ICL dynamics, we recompute these quantities independently at each in-context position using the class-conditioned record-layer representations observed at that position.

A.8 Online learning algorithms

Fix a task instance $T_{\ell,w}$. The labels $y_i = y_i^{(\ell,w)}$ are defined by this task instance, while the cognitive models operate on record-layer representations (the final layer in the main text).

Let $z_i^{(\ell,w)} \in \mathbb{R}^d$ denote the record-layer sentence representation at in-context position i , and let $\mu^{(\ell,w)}$ be the empirical mean computed jointly over all sequences and positions in the evaluated batch. We first center and normalize each representation,

$$\tilde{z}_i^{(\ell,w)} = \sqrt{d} \frac{z_i^{(\ell,w)} - \mu^{(\ell,w)}}{\|z_i^{(\ell,w)} - \mu^{(\ell,w)}\|_2},$$

and, within this subsection, suppress the task superscript when no ambiguity arises. We therefore consider the causal sequence $\{(\tilde{z}_i, y_i)\}_{i=1}^N$, where $y_i \in \{0,1\}$ is the observed label. At position i , the learner conditions on the prefix $\mathcal{D}_{<i} = \{(\tilde{z}_j, y_j)\}_{j<i}$ and produces class logits $\ell_{i,m}(c)$ for $c \in \{0,1\}$. For binary comparisons we use the logit difference $d_{i,m} = \ell_{i,m}(1) - \ell_{i,m}(0)$. The first family of models predicts by geometric similarity to previously observed examples, whereas the second maintains a parametric state that is updated after each labeled observation.

A.8.1 Similarity-based models.

Let $\mathcal{I}_{<i,c} = \{j < i : y_j = c\}$ and define the normalized squared distance $\delta(u, v) = \frac{1}{d} \|u - v\|_2^2$. These models score a class by how close the current representation is to previously observed members of that class. When $\mathcal{I}_{<i,c} = \emptyset$, the class has not yet been observed and its score is undefined, so we set $\ell_{i,m}(c) = -\infty$. Although these models are usually introduced as hard classifiers, here we retain their class scores as logits so they can be temperature-scaled and compared directly to the LLM probabilities (Subsubsection A.8.3). In the binary case we therefore fit them only at positions where both classes have been observed, so that $d_{i,m}$ is finite.

Prototype. Define the class centroid

$$m_{<i,c} = \frac{1}{|\mathcal{I}_{<i,c}|} \sum_{j \in \mathcal{I}_{<i,c}} \tilde{z}_j, \quad \ell_{i,\text{proto}}(c) = -\delta(\tilde{z}_i, m_{<i,c}).$$

Exemplar.

$$S_{<i,c} = \log \sum_{j \in \mathcal{I}_{<i,c}} \exp(-\delta(\tilde{z}_i, \tilde{z}_j)), \quad \ell_{i,\text{ex}}(c) = S_{<i,c},$$

which corresponds to a kernel density estimate over stored exemplars with a fixed bandwidth (a global rescaling is absorbed by the temperature fit).

1-nearest neighbor (1NN).

$$\ell_{i,1\text{NN}}(c) = -\min_{j \in \mathcal{I}_{<i,c}} \delta(\tilde{z}_i, \tilde{z}_j).$$

A.8.2 Online linear models.

Online gradient descent (OGD). Intuitively, OGD treats \tilde{z}_i as the input to a linear classifier and nudges that classifier after each labeled example. The learner maintains weights $W_i \in \mathbb{R}^{d \times 2}$ and bias $b_i \in \mathbb{R}^2$. At position i , the predictive logits are

$$\ell_{i,\text{OGD}} = W_{i-1}^\top \tilde{z}_i + b_{i-1}, \quad p_{i-1} = \text{softmax}(\ell_{i,\text{OGD}}),$$

and after observing (\tilde{z}_i, y_i) we update

$$W_i = (1 - \lambda)W_{i-1} - \eta \tilde{z}_i (p_{i-1} - e_{y_i})^\top, \quad b_i = b_{i-1} - \eta (p_{i-1} - e_{y_i}),$$

where $e_{y_i} \in \{0, 1\}^2$ is the one-hot label vector, $\eta > 0$ is the step size, and $\lambda \geq 0$ is weight decay applied to W only. We evaluate all six combinations $\eta \in \{0.1, 0.2, 0.5\}$ and $\lambda \in \{0, 0.1\}$, and report the best-fitting variant.

Bayesian class-mean model. Intuitively, this model treats each class as having an unknown latent mean and updates a posterior over that mean online. Concretely, it assumes a Gaussian observation model $\tilde{z}_j | (y_j = c) \sim \mathcal{N}(\theta_c, \sigma^2 I)$ with prior $\theta_c \sim \mathcal{N}(0, \tau^2 I)$. Let $n_{<i,c} = |\mathcal{I}_{<i,c}|$ and $s_{<i,c} = \sum_{j \in \mathcal{I}_{<i,c}} \tilde{z}_j$. Conjugacy yields a posterior $\theta_c | \mathcal{D}_{<i} \sim \mathcal{N}(m_{<i,c}, v_{<i,c} I)$ with

$$v_{<i,c} = (\tau^{-2} + n_{<i,c} \sigma^{-2})^{-1}, \quad m_{<i,c} = v_{<i,c} \sigma^{-2} s_{<i,c}.$$

Writing

$$\pi_{<i,c} = \frac{n_{<i,c} + 1}{\sum_{c'} n_{<i,c'} + 2},$$

for the Dirichlet(1) class prior, the predictive logits are

$$\ell_{i,\text{Bayes}}(c) = -\frac{\delta(\tilde{z}_i, m_{<i,c})}{2(\sigma^2 + v_{<i,c})} - \frac{1}{2} \log(\sigma^2 + v_{<i,c}) + \log \pi_{<i,c}.$$

This is a dimension-normalized predictive score, so both the distance term and uncertainty penalty are expressed per feature dimension. When $i = 1$, all class scores are equal up to constants and we set $\ell_{1,\text{Bayes}}(c) = 0$. We sweep $\tau^2 \in \{0.1, 0.5, 1\}$ and $\sigma^2 \in \{0.5, 1\}$, and we

also evaluate a Student- t predictive variant. The resulting fits are very similar, so we report the best-fitting Bayesian class-mean model.

Kalman filter. Intuitively, the Kalman filter maintains a linear decoder together with an uncertainty matrix that determines how strongly each new example should change the current decoder. Let $y_i \in \{0, 1\}$ denote the observed class and define the transformed target vector $u_i \in \{-1, +1\}^2$ by $u_{i,c} = 2\mathbb{I}[y_i = c] - 1$. The learner maintains weights $W_i \in \mathbb{R}^{d \times 2}$ and a covariance matrix $P_i \in \mathbb{R}^{d \times d}$ with prior $W_0 = 0$ and $P_0 = \alpha I$. At time i , it predicts $\ell_{i,\text{Kalman}} = W_{i-1}^\top \tilde{z}_i$ and updates

$$K_i = \frac{P_{i-1} \tilde{z}_i}{\sigma^2 + \tilde{z}_i^\top P_{i-1} \tilde{z}_i}, \quad W_i = W_{i-1} + K_i (u_i - \ell_{i,\text{Kalman}})^\top, \quad P_i = P_{i-1} - K_i \tilde{z}_i^\top P_{i-1}.$$

We sweep $\alpha \in \{0.1, 1\}$ and $\sigma^2 \in \{0.1, 1\}$. Differences are small, so we report the best-fitting Kalman filter.

A.8.3 Model fitting

We compare cognitive models at the level of their induced probabilities over score tokens. Each model outputs logits $\ell_{i,m}(c)$ which are mapped to probabilities by temperature scaling,

$$p_{i,m}(c) = \text{softmax}(\beta_m \ell_{i,m})_c,$$

with a single fitted inverse temperature $\beta_m \in \mathbb{R}$ per model variant and task instance. In the binary case, this reduces to $p_{i,m}(1) = \sigma(\beta_m d_{i,m})$.

To match the LLM’s probabilistic outputs, we fit β_m in log-odds space. Let $p_i^{\text{LLM}}(c)$ denote the LLM’s probability of emitting score token c (obtained from the score-position logits) and define the LLM log-odds $g_i = \log p_i^{\text{LLM}}(1) - \log p_i^{\text{LLM}}(0)$. For each model, define its logit difference $d_{i,m} = \ell_{i,m}(1) - \ell_{i,m}(0)$. For binary choice, the temperature is identifiable and admits a closed-form least-squares solution,

$$\beta_m^* = \arg \min_{\beta} \sum_i (g_i - \beta d_{i,m})^2 \quad \Rightarrow \quad \beta_m^* = \frac{\sum_i d_{i,m} g_i}{\sum_i (d_{i,m})^2}.$$

For model families with internal hyperparameters, we apply this same fitting procedure to every candidate variant in the grids above and retain the variant with the best descriptive fit. We report descriptive fit to the LLM using β_m^* (e.g., agreement after temperature scaling).